



**MICROSTRUCTURAL CHARACTERIZATION OF
PRESSURELESS SINTERED SILVER DIE ATTACHED
MATERIAL**



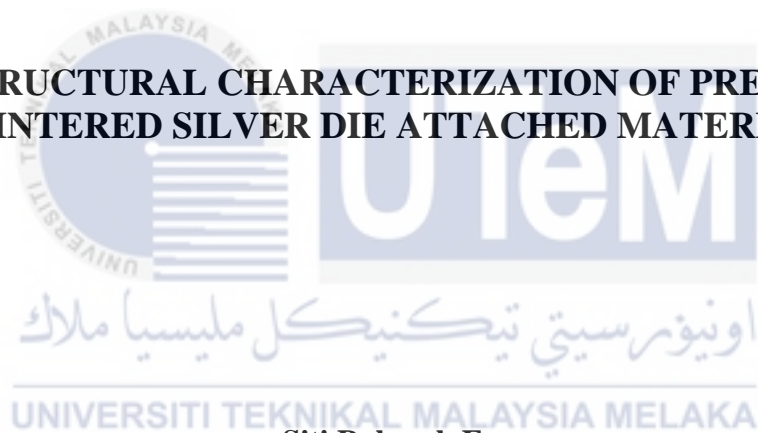
DOCTOR OF PHILOSOPHY

2022



Faculty of Mechanical Engineering

**MICROSTRUCTURAL CHARACTERIZATION OF PRESSURELESS
SINTERED SILVER DIE ATTACHED MATERIAL**



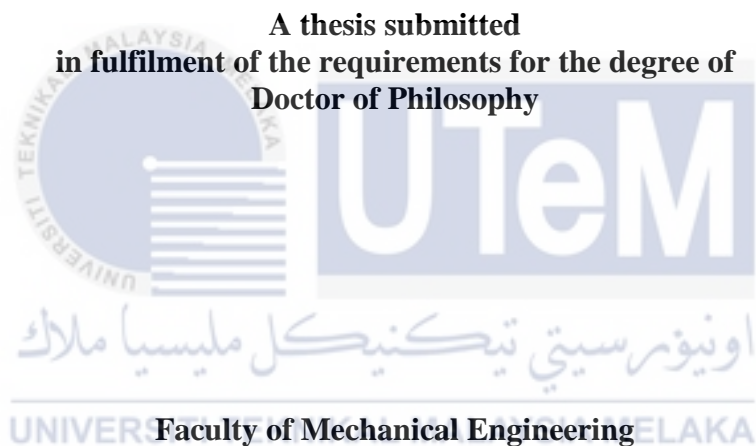
Siti Rahmah Esa

Doctor of Philosophy

2022

**MICROSTRUCTURAL CHARACTERIZATION OF PRESSURELESS SINTERED
SILVER DIE ATTACHED MATERIAL**

SITI RAHMAH ESA





UNIVERSITI TEKNIKAL MALAYSIA MELAKA

2022


DECLARATION

I declare that this thesis entitled “Microstructural Characterization Of Pressureless Sintered Silver Die Attached Material” is the result of my own research except as cited in the references. The thesis has not been accepted for any degree and is not concurrently submitted in candidature of any other degree.

 
Signature :
Name : Siti Rahmah Esa
Date : 19/09/2022
اونشيتي تیکنیکل ملیسيا ملاک
UNIVERSITI TEKNIKAL MALAYSIA MELAKA

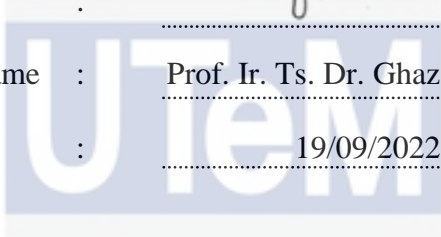

APPROVAL

I hereby declare that I have checked this thesis and in my opinion, this thesis is sufficient in terms of scope and quality for the award of the degree of Doctor of Philosophy.

Signature : 

Supervisor Name : Prof. Ir. Ts. Dr. Ghazali Omar

Date : 19/09/2022



اونيورسيتي تيكنيكل مليسيا ملاك
UNIVERSITI TEKNIKAL MALAYSIA MELAKA

DEDICATION

To my beloved parents; Haji Esa Idrus and Hajah Saadiyah Safar.

To my beloved siblings; Sabariah, Salamiah, Siti Saharah, Fuad and Umi Kalsom.

To my brother and sister in law; David Appleton and Zuraidah.

To my niece and nephew; Layla Asifa, Naura Imani, Neuman, and Niklaus Appleton.

To my co-worker in MIMOS Semiconductor (M) Sdn Bhd.

Thank you for all the support that I finally made it to finish my thesis.



ABSTRACT

Sintered silver (Ag) is one of the most promising interconnect materials for high power electronics applications due to its ability to withstand high temperature exceeding 250 °C while in operation. In this thesis, the microstructural evolutions of spherical and flake types pressureless sintered Ag die attached material was characterized at different sintering temperatures. The interface between flake sintered Ag and copper (Cu) substrate was examined to understand the factor that affects its bonding quality. The flake sintered Ag was exposed to corrosive environment to study the effect of corrosion to its properties change. The microstructural characterization was performed by means of field emission scanning electron microscopy (FESEM), focused ion beam (FIB) and high resolution transmission electron microscopy (HRTEM). The elemental and chemical states analysis were performed via energy dispersive spectroscopy (EDS), x-ray photoelectron spectroscopy (XPS) and time of flight secondary ion mass spectrometry (TOF-SIMS). The mechanical properties was conducted using dynamic microhardness tester and the electrical conductivity was measured using hall effect instrument. The result shows that the evolutions of spherical particles occur as the contact area is formed, followed by neck formation via atomic diffusions leading to the formation of solid Ag network. The flake particles shows self-produced nano particles that accelerates the sintering process and it has a higher tendency for particle diffusions due to larger surface area per thickness ratio. The improvement in conductivity was observed as compared with unsintered Ag particles. The flake Ag particle sintered at 300 °C shows an increase in elastic modulus and hardness as compared to unsintered Ag particle. The investigation at the interface between sintered Ag and Cu substrate shows an indication of interface diffusion after the sintering process. However, the growth of Cu oxide layer at Ag-Cu interfaces induce negative effects due to the formation of voids and separations in between Cu and Cu oxide interface. Finally, the evidence of corroded sintered Ag joint was observed after exposure to the corrosive environment. The Cu oxide layer with delamination between Cu and Cu oxide interface initiate a weak point and further enhance the corrosion effect. The corrosion and delamination will result in product failure due to poor mechanical strength of the corroded joints. In conclusion, sintering temperature plays an important role in the microstructural change of sintered Ag joint. The knowledge gained from this study would be beneficial in the application of pressureless sintered Ag die attached material in semiconductor packaging process.

PENCIRIAN STRUKTURMIKRO BAHAN PELEKAT CIP PERAK DISINTER TANPA TEKANAN

ABSTRAK

Perak tersinter ialah salah satu bahan penghubung yang paling utama untuk aplikasi elektronik berkuasa tinggi kerana keupayaannya untuk menahan suhu tinggi melebihi 250 °C semasa beroperasi. Dalam tesis ini, evolusi strukturmikro bahan pelekak cip perak disinter tanpa tekanan telah dicirikan pada suhu pensinteran yang berbeza. Permukaan antara kepingan perak tersinter dan substrat tembaga diperiksa untuk memahami faktor yang mempengaruhi kualiti ikatannya. Kepingan perak tersinter kemudiannya didedahkan kepada persekitaran menghakis untuk mengkaji kesan ion menghakis terhadap perubahan sifatnya. Pencirian strukturmikro dilakukan dengan menggunakan mikroskop elektron pengimbas pelepasan medan (FESEM), pancaran ion fokus (FIB) dan mikroskop transmisi elektron beresolusi tinggi (HRTEM). Analisis keadaan unsur dan kimia dilakukan melalui kaedah spektroskopi penyebaran tenaga (EDS), spektroskopi fotoelektron sinar-x (XPS) dan masa penerbangan spektrometri jisim ion sekunder (TOF-SIMS). Sifat mekanik diuji dengan menggunakan penguji dinamik kekerasanmikro dan kekonduksian elektrik diukur dengan menggunakan instrumen kesan medan. Hasilnya menunjukkan bahawa evolusi zarah sfera berlaku apabila kawasan sentuhan terbentuk, diikuti dengan pembentukan leher melalui resapan atom yang membawa kepada pembentukan rangkaian perak yang padat. Zarah nano yang terhasil pada kepingan perak mempercepatkan proses pensinteran dan ia mempunyai kecenderungan yang lebih tinggi untuk resapan zarah disebabkan oleh luas permukaan yang lebih besar berbanding dengan partikel sfera. Nilai kekonduksian didapati meningkat berbanding dengan partikel perak yang tidak disinter. Kepingan perak yang disinter pada 300 °C menunjukkan peningkatan dalam modulus anjal dan kekerasan berbanding dengan kepingan perak yang tidak disinter. Penyiasatan pada permukaan perak tersinter dan substrat tembaga menunjukkan berlakunya resapan antara muka selepas proses pensinteran. Walau bagaimanapun, pertumbuhan lapisan tembaga oksida pada permukaan perak-tembaga mendorong kesan negatif akibat pembentukan lompong dan pemisahan di permukaan tembaga dan tembaga oksida. Akhirnya, bukti kakisan pada perak tersinter diperhatikan selepas terdedah kepada persekitaran yang menghakis. Pemisahan pada permukaan tembaga dan tembaga oksida menghasilkan titik lemah dan meningkatkan lagi kesan kakisan. Kakisan dan pemisahan akan mengakibatkan kegagalan produk kerana kekuatan mekanikal menjadi lemah pada sendi yang terhakis. Kesimpulannya, suhu pensinteran memainkan peranan yang penting dalam perubahan strukturmikro perak tersinter. Pengetahuan yang diperolehi daripada kajian ini akan memberi manfaat dalam penggunaan bahan pelekak cip perak tersinter tanpa tekanan dalam proses pembungkusan semikonduktor.

ACKNOWLEDGEMENT

In the Name of Allah, the Most Gracious, the Most Merciful

First and foremost, I would like to thank and praise Allah the Almighty, my Creator, my Sustainer, for everything I received since the beginning of my life. I would like to extend my appreciation to Universiti Teknikal Malaysia Melaka (UTeM) for providing the research platform.

My utmost appreciation goes to my main supervisor, Prof. Ir. Ts. Dr. Ghazali Omar for his continuous support, motivation, encouragement and guidance, which I am truly grateful. His constant patience in guiding and providing priceless insights will forever be remembered. Also, to my co-supervisor, Dr. Siti Hajar Sheikh Md Fadzullah for her support of my research work. My special thanks go to Dr. Shutesh Krishnan (On Semiconductor (M) Sdn Bhd) and Dr. Kim Siow Shyong (Universiti Kebangsaan Malaysia) for all the help and support I received from them. I also would like to thank the management of MIMOS Semiconductor (M) Sdn Bhd, in particular Mr. Wan Azli Wan Ismail, Mrs. Bazura Abdul Rahim and members in Advanced Analytical Services Laboratory for supporting this research work.

Last but not least, from the bottom of my heart, a gratitude to my beloved parents and my siblings for their endless support, love and prayers. Finally, thank you to all the individuals who had provided me the assistance, support and inspiration which made it possible for me to complete this research work and thesis write-up.

TABLE OF CONTENTS

	PAGE
DECLARATION	
APPROVAL	
DEDICATION	
ABSTRACT	i
ABSTRAK	ii
ACKNOWLEDGEMENT	iii
TABLE OF CONTENTS	iv
LIST OF TABLES	vii
LIST OF FIGURES	ix
LIST OF ABBREVIATIONS	xvii
LIST OF SYMBOLS	xix
LIST OF APPENDICES	xxii
LIST OF PUBLICATIONS	xxiii
CHAPTER	
1. INTRODUCTION	1
1.1 Background	1
1.2 Problem Statements	3
1.3 Research Objectives	5
1.4 Scopes of Research	5
1.5 Contributions of Research	6
1.6 Significant of Research	7
1.7 Thesis Outlines	8
2. LITERATURE REVIEW	10
2.1 Semiconductor Packaging	10
2.2 Die Attach Technology for Semiconductor Packaging	11
2.2.1 Die Attach Materials	12
2.2.2 Epoxy Die Attach	13
2.2.3 Solder Die Attach	13
2.2.4 Eutectic Die Attach	15
2.2.5 Sintered Ag Die Attach	16
2.2.6 Comparison between Ag Sintering and Soldering	20
2.3 Sintering	21
2.3.1 Sintering of Ag	24
2.3.2 Sintering Variables	26
2.3.2.1 Material Variables	26
2.3.2.2 Process Variables	27
2.4 Sintering Driving Force	28
2.4.1 Surface Energy	28
2.4.2 Particle Size	31
2.5 Densification and Grain Growth	32

2.6	Sintering Stages	33
2.6.1	Initial Stage	34
2.6.2	Intermediate Stage	34
2.6.3	Final Stage	35
2.7	Sintering Material Transport Mechanism	36
2.8	Diffusion Mechanism Controlling Solid State Sintering Process	38
2.8.1	Lattice Diffusion	38
2.8.2	Grain Boundary Diffusion	39
2.8.3	Surface Diffusion	41
2.9	Review of Previous Studies	42
2.9.1	Pressure-Assisted and Pressureless Ag sintering	45
2.9.2	Microstructural Evolution and Porosity of Pressureless Sintered Ag	46
2.9.3	Sintered Ag Interfacial Bonding	48
2.9.4	Corrosion Issue in Sintered Ag	49
2.9.5	Summary	50
3.	MATERIALS AND METHODOLOGY	51
3.1	Ag Paste Materials	51
3.2	Substrate Material	54
3.3	Sample Preparation	55
3.3.1	Sample Preparation for Microstructural Characterization of Sintered Ag	57
3.3.2	Sample Preparation for Interfacial Reaction Study	60
3.3.3	Sample Preparation for Environmental Effect to the Sintered Ag	62
3.4	Characterization Procedure	64
3.4.1	Surface Texture and Morphology Characterization	69
3.4.2	Surface Roughness Characterization	72
3.4.3	Internal Microstructure Characterization	73
3.4.4	Particle and Grain Size Measurement	75
3.4.5	Neck Width Measurement	76
3.4.6	Porosity Measurement	77
3.4.7	Hardness Test Measurement	79
3.4.8	Conductivity and Resistivity	82
3.4.9	Characterization at Interface	84
3.4.10	HRTEM Characterization	84
3.4.11	Elemental Characterization	88
3.4.12	XPS Characterization	91
3.4.13	TOF-SIMS Characterization	95
4.	RESULTS AND DISCUSSION	98
4.1	Unsintered Ag Particle and Pressureless Sintered Ag	98
4.1.1	Ag Particle Geometry, Size and Distributions Prior to Sintering	98
4.1.2	Microstructure of Ag Particles Prior to Sintering	101
4.1.3	Elemental Compositions of Ag Paste Material	104
4.1.4	Surface Interaction and Diffusions after Sintering	105
4.1.5	Surface Roughness Change after Sintering	111

4.1.6	Surface Elemental Composition via XPS analysis after Sintering	113
4.1.7	Bulk Properties of Ag Particle and Grain Size Growth after Sintering	116
4.1.8	Necking Formation and Growth after Sintering	122
4.1.9	Pore Formation after Sintering	124
4.1.10	Mechanism of Pore Formation	128
4.1.11	Conductivity and Resistivity	132
4.2	Ag Flake Particles and Interface Study between Sintered Ag and Cu Substrate	134
4.2.1	Ag Particle Geometry and Dimension prior to Sintering	134
4.2.2	Surface Nucleation on Sintered Micron-Sized Ag flakes	138
4.2.3	Bulk Properties of Sintered Micron-Sized Ag flakes	143
4.2.4	Comparison between Sintering on Spherical and Flake Geometry	146
4.2.5	Pressureless Sintered Ag on Cu Substrate	151
4.2.6	Porosity Analysis of Sintered Ag on Cu Substrate	156
4.2.7	XPS Surface Analysis of Sintered Ag on Cu Substrate	160
4.2.8	Effect of Mechanical Testing to the Microporous Sintered Ag on Cu Substrate	166
4.2.9	Effect of Electrical Conductivity and Resistivity on Microporous Sintered Ag	174
4.2.10	Interface Study between Sintered Ag and Cu Substrate	176
4.2.11	Cu Oxidation	185
4.3	Corrosion Behavior of Sintered Ag	194
4.3.1	Effect of Corrosion on Sintered Ag Surface	194
4.3.2	Effect of Corrosion to the bulk properties of Sintered Ag	198
4.3.3	Effect of Corrosion at the interface between Ag-Cu	202
4.3.4	XPS analysis on Sintered Ag after Exposed to NaCl Solution	204
4.3.5	TOF-SIMS analysis on Sintered Ag after Exposed to NaCl	211
4.3.6	Effect of Corrosion to the modulus of elasticity	229
4.3.7	AgCl Corrosion Layer	231
5.	CONCLUSION AND RECOMMENDATIONS	233
5.1	Conclusion	233
5.2	Recommendation	235
	REFERENCES	236
	APPENDICES	269

LIST OF TABLES

TABLE	TITLE	PAGE
2.1	Main events during bonding formations of Ag sintering and soldering (Chen and Zhang, 2019)	20
2.2	The mechanism of material transport during sintering	37
2.3	The summary of the prior works	43
3.1	Material properties of Ag paste according to the technical data sheet provided by the supplier	53
3.2	The list of samples on Si substrate for pressureless sintering process	59
3.3	The list of samples on Cu substrate for pressureless sintering process	61
3.4	The list of samples for the effect of corrosive environment	63
4.1	The elemental compositions on the sample surface	114
4.2	The elemental compositions on the surface of unsintered and sintered Ag samples	161
4.3	The elastic modulus and hardness values of unsintered and sintered samples	172
4.4	The average of Cu oxide thickness	179
4.5	The elemental compositions on the surface of untreated and heat treated Ag samples	190
4.6	The elemental compositions on sample surface after exposure to NaCl	206
4.7	The peak list of ion detections in positive polarity	218
4.8	The peak list of ionic compounds detected in positive polarity	219
4.9	The peak list of hydrocarbon detections in positive polarity	220

4.10	The peak list of ion detections in negative polarity	221
4.11	The peak list of ion detections at higher mass range in negative polarity	222
4.12	The elastic modulus and hardness values of samples after exposure to NaCl	230



LIST OF FIGURES

FIGURE	TITLE	PAGE
2.1	The schematic of IC package (Graycochea et al., 2020)	11
2.2	The illustration of heat conduction path between sintered Ag and Ag epoxy die attach (Hueners et al., 2019)	17
2.3	Die attach material platform for various ranges of power electronic applications (Zhang and Sukanuma, 2019)	19
2.4	FESEM micrograph of sintered bronze particles (Banhart, 2001)	22
2.5	The illustration of sintering mechanism based on two particle's model (Drescher and Seitz, 2015)	23
2.6	The illustration of driving force for sintering (Kang, 2004)	30
2.7	The relationship between particle size and total surface area (Peng et al., 2015)	31
2.8	The densification curve during sintering stages (Exner and Artz, 1990)	33
2.9	The illustration of necking formation and growth (Rojek et al., 2017)	34
2.10	Coble's model of (a) intermediate and (b) final sintering stage (Coble, 1990)	35
2.11	Mechanism of material transport during sintering (Kang, 2004)	37
2.12	Electron micrograph image of the grain structure and grain boundary in a polycrystalline material	39
2.13	The illustration of grain boundary diffusion (Herzig and Mishin, 2005)	40
3.1	The as-received Ag paste materials from the suppliers	52
3.2	Sintering profile as recommended by the suppliers	54

3.3	Substrate materials of (a) Si wafer and (b) Cu leadframe	55
3.4	The process flow of sample preparation procedures	56
3.5	(a) A cleaved Si substrate and (b) Si substrate after printed with Ag paste	57
3.6	The high temperature oven used for the sintering process	58
3.7	(a) Cu substrate and (b) Cu substrate after printed with Ag paste	60
3.8	Ag paste sample that was soaked in NaCl solution	62
3.9	The process flow of characterization procedures	68
3.10	Dual Beam equipment	69
3.11	Illustration of electron-sample interactions on sample surface (Akhtar et al., 2018)	71
3.12	Illustration of secondary electron emission (UI Hamid, 2018)	72
3.13	Stylus profilometer equipment	72
3.14	FIB cross-sectioning from the top view	75
3.15	The illustration of maximum feret diameter measurement	76
3.16	The measurement of neck width between two connecting particles	77
3.17	The binary image converted using Image J software for porosity calculation	78
3.18	Dynamic micro hardness tester	79
3.19	The illustration of FIB cut procedure from top view of Berkovich indentation mark on sintered Ag sample	82
3.20	Hall effect equipment	83
3.21	Sample mounted on the stage of hall effect instrument	83
3.22	The illustration of interface region between sintered Ag and Cu leadframe substrate	84
3.23	The TEM lamella preparation steps	86
3.24	HRTEM equipment	87
3.25	Electron-sample interactions on thin sections (Dey, 2018)	88
3.26	The EDS detector	89
3.27	The principle of x-ray emission (Hodoroaba, 2020)	90
3.28	XPS equipment	91
3.29	The illustration of photoemission process (Haasch, 2014)	92
3.30	(a) XPS survey scan and (b) narrow scan spectra of sintered Ag (Khtatba et al., 2018)	94

3.31	TOF-SIMS equipment	95
3.32	The illustration of TOF-SIMS principle (Bonnin and Rizzoli, 2020)	97
4.1	Electron micrograph captured from the top view of the sample shows the distributions and geometry of Ag particles prior to sintering	99
4.2	Electron micrograph captured from cross-sectional view of the sample prior to sintering	99
4.3	Particle size distributions prior to sintering	100
4.4	HRTEM micrographs of Ag particles prior to sintering. (a) Microstructure of crystalline Ag particles, (b) nano-sized Ag particles observed on polymeric material, (c) magnified view of nano-sized Ag particles, (d) HRTEM shows the grain boundary and lattice spacing of 0.2 nm, and (e) the corresponding FFT pattern	103
4.5	(a) STEM micrograph indicated the EDS elemental mapping region within the orange box, (b) blue colour represent the Ag element, (c) red colour represent the C element, and (d) green colour represent the O element	104
4.6	The comparison of surface interaction between Ag particles at (a) RT, (b) 100 °C, (c) 200 °C, (d) 250 °C, (e) 275 °C, and (f) 300 °C sintering temperature	107
4.7	Magnified FESEM micrograph for (a) RT, (b) 100 °C, (c) 200 °C, (d) 250 °C, (e) 275 °C, and (f) 300 °C sintering temperature	109
4.8	Histogram of surface grain size for (a) RT, (b) 100 °C, (c) 200 °C, (d) 250 °C, (e) 275 °C, and (f) 300 °C sintering temperature	110
4.9	The RMS value for sample at RT and after sintered	111
4.10	3D surface roughness micrograph of (a) RT, (b) 100 °C, (c) 200 °C, (d) 250 °C, (e) 275 °C, and (f) 300 °C sintering temperature	112
4.11	XPS survey scan spectra of (a) RT, (b) 250 °C, (c) 275 °C, and (d) 300 °C sintering temperature	113
4.12	XPS chemical state analysis of sample at RT	115
4.13	XPS chemical state analysis of sample sintered at 300 °C	116
4.14	The FIB micrographs for sample at (a) 200 °C, (b) 250 °C, (c) 275 °C, and (d) 300 °C sintering temperature	117

4.15	The sintering mechanism of Ag particles (a) Ag particles initiate intimate contact, (b) initiation of surface diffusion, (c) necking growth, (d) particle growth, and formation of a solid Ag network	118
4.16	The average particle size at 200 °C, 250 °C, and 275 °C sintering temperature	120
4.17	The average grain size at 200 °C, 250 °C, 275 °C, and 300 °C sintering temperature	120
4.18	The average neck width at different sintering temperature	123
4.19	The average neck growth ratio at different sintering temperature	123
4.20	The corresponding binary image and automated pore size calculation using Image J	125
4.21	The porosity after exposure at different sintering temperature	126
4.22	The pore size after exposure at different sintering temperature	126
4.23	The mechanism of pore formation (Fang, 2010; Van Nguyen et al., 2016)	129
4.24	Large pores at 35000 magnification	130
4.25	Small pores at 150000 magnification	131
4.26	Illustration of (a) high grain coordination inhibited densification and (b) low grain coordination continued densification (German, 2014)	131
4.27	The conductivity of sintered Ag at different sintering temperature	133
4.28	The resistivity of sintered Ag at different sintering temperature	133
4.29	FESEM micrograph of samples that was dried at room temperature. (a) micron flake Ag particles, (b) spherical Ag particle, (c) FIB cross-sectioned of micron flake Ag particles, and (d) FIB cross-sectioned of spherical Ag particles	136
4.30	(a) EDS spectra of micron flake Ag particles and (b) EDS mapping shows the presence of Ag element as indicated in green colour	137
4.31	Particle distribution of Ag flake prior to sintering	137
4.32	The comparison of contact points between (a) spherical particles and (b) flake particle (Yao et al., 2018)	138
4.33	FESEM micrograph of Ag flake that was sintered at (a) 200 °C, (b) 250 °C, (c) 275 °C, and (d) 300 °C	140

4.34	FESEM micrograph of Ag flake that was sintered at (a) 200 °C, (b) 250 °C, (c) 275 °C, and (d) 300 °C	141
4.35	Histogram distribution of nano particle size of Ag flake that was sintered at (a) 250 °C, (b) 275 °C, and (c) 300 °C	142
4.36	FIB cross-sectioned of Ag flake that was sintered at (a) 200 °C, (b) 250 °C, (c) 275 °C, and (d) 300 °C	144
4.37	Histogram distribution of Ag flake thickness after sintered at (a) 200 °C, (b) 250 °C, (c) 275 °C, and (d) 300 °C	145
4.38	Sample that was sintered at 250 °C; top view of (a) spherical, (b) flake and FIB cross-sectioned view of (c) spherical, (d) flake	147
4.39	Sample that was sintered at 300 °C; top view of (a) spherical, (b) flake and FIB cross-sectioned view of (c) spherical, (d) flake	149
4.40	The mechanism of pore formation between spherical and flake particles geometry (Fu et al., 2018)	150
4.41	TEM image of initial Ag flake particle	151
4.42	FIB cross-sectioned micrograph of Ag paste that was deposited on bare Cu substrate and dried at room temperature (a) overview and (b) magnified view	152
4.43	Sintered Ag on Cu substrate at (a) 200 °C, (b) 250 °C, (c) 275 °C, and (d) 300 °C	154
4.44	Two regions with the variation of particle size denoted with A and B on the sample that was sintered at 300 °C	155
4.45	Pore area generated using Image J software for (a) unsintered sample, (b) 200 °C, (c) 250 °C, (d) 275 °C, and (e) 300 °C	157
4.46	The porosity of unsintered and sintered Ag at 200 °C, 250 °C, 275 °C, and 300 °C	157
4.47	The pore size of unsintered and sintered Ag at 200 °C, 250 °C, 275 °C, and 300 °C	158
4.48	XPS survey scan spectra of (a) RT, (b) 200 °C, (c) 250 °C, (d) 275 °C, and (e) 300 °C sintering temperature	160
4.49	XPS chemical state analysis of unsintered Ag flake sample	162
4.50	XPS chemical state analysis of Ag flake sample sintered at 200 °C	163
4.51	XPS chemical state analysis of Ag flake sample sintered at 250 °C	164

4.52	XPS chemical state analysis of Ag flake sample sintered at 275 °C	164
4.53	XPS chemical state analysis of Ag flake sample sintered at 300 °C	165
4.54	Tilted view FIB micrograph of micro-indentation on sintered Ag at (a) 200 °C, (b) 250 °C, (c) 275 °C, and (d) 300 °C	167
4.55	Cross-sectional FIB micrograph of micro-indentation on sintered Ag at (a) 200 °C, (b) 250 °C, (c) 275 °C, and (d) 300 °C	169
4.56	Magnified FIB cross-sectional micrograph underneath the indented region of 300 °C sample shows the evidence of no fracture nor crack at the necking area of the sintered structure	170
4.57	Load-displacement curve for three types of materials (a) high elastic, (b) plastic properties, and (c) elastically recovered during unloading (Hainsworth et al., 1996)	170
4.58	Applied load versus displacement curve obtained via dynamic microhardness test	171
4.59	The conductivity of sintered Ag at different sintering temperature	174
4.60	The resistivity of sintered Ag at different sintering temperature	175
4.61	FIB cross-sectional micrograph at Ag-Cu interface of unsintered sample	177
4.62	FIB cross-sectional micrograph of Ag-Cu interface sintered at (a) 200 °C, (b) 250 °C, (c) 275 °C, and (d) 300 °C	178
4.63	The copper oxide thickness growth on sintered samples	180
4.64	Magnified FIB cross-sectional micrograph of Ag-Cu interface sintered at (a) 200 °C, (b) 250 °C, (c) 275 °C, and (d) 300 °C	181
4.65	Inter-diffusion between Ag and Cu oxide interface	183
4.66	EDS mapping analysis of (a) unsintered and sintered samples at (b) 200 °C, (c) 250 °C, (d) 275 °C, and (e) 300 °C. Green represent Ag element from unsintered and sintered Ag material, blue represent O element from Cu oxide layer and red represent Cu element from bare Cu substrate	184
4.67	FESEM micrograph of (a) un-treated Cu leadframe, (b) the imprint of Vickers indentation of un-treated Cu leadframe, (c) Cu leadframe after heat treated at 250 °C, and (d) the imprint of Vickers indentation on Cu leadframe after heat treated at 250 °C	186

4.68	HRTEM micrograph of Cu oxide layer	187
4.69	XPS survey scan spectra of (a) untreated and heat treated Cu substrate at (b) 200 °C, (c) 250 °C, (d) 275 °C, and (e) 300 °C	189
4.70	XPS chemical state analysis of (a) untreated and heat treated bare Cu substrate at (b) 200 °C, (c) 250 °C, (d) 275 °C, and (e) 300 °C	191
4.71	XPS depth profile of (a) untreated and heat treated Cu substrate at (b) 200 °C, (c) 250 °C, (d) 275 °C, and (e) 300 °C. Red line represent the O element, while the blue line represent the Cu element	193
4.72	Overview and magnified FESEM micrograph of pressureless sintered Ag (a) without exposure to NaCl and after exposure to NaCl solution for (b) 1 day, (c) 5 days, and (d) 10 days	196
4.73	EDS mapping result of sample exposure to NaCl for 5 days. (a) EDS spectra, (b) the EDS analysis location, (c) green colour represent Ag mapping, (d) blue colour represent Na mapping, and (e) red colour represent Cl mapping	197
4.74	FIB cross-sectioned view after immersed in NaCl for 1 day	198
4.75	FIB cross-sectioned view after immersed in NaCl for 5 days	199
4.76	FIB cross-sectioned view after immersed in NaCl for 10 days	200
4.77	EDS mapping result at the cross-sectional view of sample after exposure to NaCl for 5 days. (a) the EDS analysis location, (b) green colour represent Ag mapping, (c) blue colour represent Na mapping, and (d) red colour represent Cl mapping	201
4.78	Interface between Ag-Cu after immersed in NaCl for 1 day	202
4.79	Interface between Ag-Cu after immersed in NaCl for 5 days	203
4.80	XPS survey scan spectra after exposure to NaCl for 1 day	204
4.81	XPS survey scan spectra after exposure to NaCl for (a) 5 days and (b) 10 days	205
4.82	XPS chemical states analysis of sintered Ag after exposure to NaCl for 1 day	208
4.83	XPS chemical states analysis of sintered Ag after exposure to NaCl for 5 days	209
4.84	XPS chemical states analysis of sintered Ag after exposure to NaCl for 10 days	210

4.85	TOF-SIMS spectra in positive polarity for sample that was not exposed to NaCl solution	212
4.86	TOF-SIMS spectra in positive polarity after exposure to NaCl for 1 day	212
4.87	TOF-SIMS spectra in positive polarity after exposure to NaCl for 5 days	213
4.88	TOF-SIMS spectra in positive polarity after exposure to NaCl for 10 days	213
4.89	TOF-SIMS spectra in negative polarity for sample that was not exposed to NaCl solution	215
4.90	TOF-SIMS spectra in negative polarity after exposure to NaCl for 1 day	215
4.91	TOF-SIMS spectra in negative polarity after exposure to NaCl for 5 days	216
4.92	TOF-SIMS spectra in negative polarity after exposure to NaCl for 10 days	216
4.93	TOF-SIMS mapping in positive ion polarity on sintered Ag that was not exposed to NaCl solution	224
4.94	TOF-SIMS mapping in positive polarity on sintered Ag after exposure to NaCl for 1 day	224
4.95	TOF-SIMS mapping in positive polarity on sintered Ag after exposure to NaCl for 5 days	225
4.96	TOF-SIMS mapping in positive polarity on sintered Ag after exposure to NaCl for 10 days	225
4.97	TOF-SIMS mapping in negative ion polarity on sintered Ag that was not exposed to NaCl solution	227
4.98	TOF-SIMS mapping in negative ion polarity on sintered Ag after exposure to NaCl for 1 day	227
4.99	TOF-SIMS mapping in negative ion polarity on sintered Ag after exposure to NaCl for 5 days	228
4.100	TOF-SIMS mapping in negative ion polarity on sintered Ag after exposure to NaCl for 10 days	228
4.101	Applied load versus displacement curve obtained via dynamic microhardness test after exposure to NaCl	230

LIST OF ABBREVIATIONS

AFM	-	Atomic Force Microscopy
BCC	-	Body Centered Cubic
BLT	-	Bond Line Thickness
CCD	-	Charged Coupled Device
CPS	-	Counts Per Second
CTE	-	Coefficient of Thermal Expansion
DBC	-	Direct Bond Copper
EDS	-	Energy Dispersive X-ray Spectroscopy
ESD	-	Electro Static Discharge
FEG	-	Field Emission Gun
FESEM	-	Field Emission Scanning Electron Microscopy
FFT	-	Fast Fourier Transform
FIB	-	Focused Ion Beam
FOV	-	Field of View
FTIR	-	Fourier Transform Infra Red
GIF	-	Gatan Imaging Filter
GIS	-	Gas Injection System
HCP	-	Hexagonal Closed Packed
HRTEM	-	High Resolution Transmission Electron Microscopy
IC	-	Integrated Circuit
IGBT	-	Insulated Gate Bipolar Transistor
IMC	-	Inter-metallic Compound
ISO	-	International Organization for Standardization
LED	-	Light Emitting Diode
LMIG	-	Liquid Metal Ion Gun
LMIS	-	Liquid Metal Ion Source
MCM	-	Multi Chip Module

NA	-	Not Applicable
NIST	-	National Institute of Standards and Technology
PCB	-	Printed Circuit Board
RMS	-	Root Mean Square
RT	-	Room Temperature
SAC	-	Tin Silver Copper
SCC	-	Stress Corrosion Cracking
SMT	-	Surface Mount Technology
STEM	-	Scanning Transmission Electron Microscopy
TEM	-	Transmission Electron Microscopy
TOF-SIMS	-	Time of Flight - Secondary Ion Mass Spectrometry
UV	-	Ultra Violet
WBG	-	Wide Band Gap
XPS	-	X-ray Photoelectron Spectroscopy

